# Characterising the surface and interior chemistry of core-shell nanoparticles using scanning transmission electron microscopy

**B. G. Mendis[1] and A. J. Craven[2,3]**

1 *Deparment. of Physics, Durham University, South Road, Durham, DH1 3LE, UK*
2 *Department of Physics and Astronomy, University of Glasgow, Glasgow, G12 8QQ, UK*
3 *SuperSTEM, Daresbury Laboratory, Keckwick Lane, Daresbury, WA4 4AD, UK*

## Abstract

A method for extracting core and shell spectra from core-shell particles with varying core to shell volume fractions is described. The method extracts the information from a single EELS spectrum image of the particle. The distribution of O and N was correctly reproduced for a nanoparticle with a TiN core and Ti-oxide shell. In addition, the O distribution from a nanoparticle with a Cu core and a Cu-oxide shell was obtained, and the extracted Cu $L_{2,3}$-core and shell spectra showed the required change in EELS near edge fine structure. The extracted spectra can be used for multiple linear least squares fitting to the raw data in the spectrum image. The effect of certain approximations on numerical accuracy, such as treating the nanoparticle as a perfect sphere, as well as the intrinsic detection limits of the technique have also been explored. The technique is most suitable for qualitative, rather than quantitative, work.

## 1. Introduction

Many materials contain a surface layer (i.e. a 'shell') that has a different composition or crystal structure to that of the interior (i.e. the 'core'). Such core-shell structures are frequently found in nanotechnology in the form of nanoparticles or nanowires [1-6]. To investigate the structure, and composition of such materials with high spatial reolution, techniques such as energy dispersive X-ray (EDX) spectroscopy and electron energy loss spectroscopy (EELS) in a scanning transmission electron microscope (STEM) are routinely used. However, due to the fact that the electrons penetrate through the specimen, the EDX and EELS signals will almost always contain information from both the core and shell regions. In such cases, multiple linear least squares (MLLS) fitting can be used to model the measured signal as a linear combination of reference spectra. For a core-shell nanoparticle, the reference spectra represent the signals from pure core and pure shell regions and are typically acquired from representative bulk materials under the same experimental conditions (i.e. specimen thickness, microscope parameters etc.). Provided the reference spectra are suitably normalised, the MLLS fit coefficient is proportional to the fraction of core or shell region within the analytical volume. Although MLLS has been highly successful in some cases (see for example [7-9]) it has the disadvantage that it is not always possible to obtain suitable reference spectra. An example is a metastable core or shell phase that is difficult to reproduce in bulk form. Furthermore knowledge of the phases that make up the core and shell material is required prior to MLLS fitting.

A new analytical method for extracting interfacial and matrix spectra from a rough interface (i.e. an interface that has projected width when viewed 'end-on') has been developed by Mendis *et al.* [10]. Similar principles can be used in the characterisation of

core-shell nanoparticles. In spectrum imaging in the STEM [11], an EELS and/or EDX spectrum is acquired at each point within a region of interest by scanning the electron probe in a controlled manner. Sub-regions within the parent spectrum image can then be selected which have varying core to shell volume fractions. Integrated spectra from sub-regions with a high core to shell volume fraction will appear more core-like while those from sub-regions with a low core to shell volume fraction will appear more shell-like. As will be shown later, this variation in the integrated spectrum can be used to extract the spectra for the pure core and pure shell regions respectively. Unlike MLLS fitting, the analysis does not require the use of reference spectra from bulk standards.

In this paper, the above mentioned analytical method is used to characterise core-shell nanoparticles. The materials systems analysed are TiN nanoparticles with a Ti-oxide shell and Cu nanoparticles with a Cu-oxide shell. Either EDX or EELS spectra could be used in the analysis but, in this study, only EELS data are presented. Apart from identifying the chemical elements that make up the solid, the energy loss near edge structure (ELNES) of the edges in the EELS spectra also provide information on the bonding environment of the ionised atom, thereby making it a powerful characterisation tool [12]. In section 2 of this paper, the mathematical background to the analytical method is presented. Section 3 contains a description of the experimental methods used while the results of the EELS analysis of core-shell nanoparticles are presented in section 4. Sources of error in the analytical model, such as the assumption of a spherically shaped nanoparticle, as well as detection limits are discussed in section 5. The summary and conclusions are presented in section 6.

## 2. Mathematical background

Let the EELS signal, acquired over an analysis region that contains volumes $V_{\text{core}}$ of core material and $V_{\text{shell}}$ of shell material be denoted by $M(E)$, where $E$ is the electron energy loss. The analysis volume is typically a sub-region from a parent spectrum image and $M(E)$ is obtained by summing the EELS spectra from each pixel within the sub-region. $M(E)$ contains contributions from the core and shell which obey a rule of mixtures, i.e.:

$$M(E) = V_{\text{core}} C(E) + V_{\text{shell}} S(E) \quad \ldots (1)$$

where $C(E)$ and $S(E)$ are the EELS signals *per unit volume* from the pure core and the pure shell regions respectively. For the analysis, it is assumed that the parent spectrum image is recorded as a straight line passing through the centre of an idealised, spherical nanoparticle viewed in projection. Sub-regions in the form of line segments symmetrical about the origin of the nanoparticle can be extracted from the parent spectrum image. Figure 1 shows the circular cross-section of a spherical nanoparticle that contains a shell of constant thickness '$h$' and a core region of radius '$R$'. The $z$-axis is parallel to the electron optic axis and the spectrum image is acquired along the $y$-direction such that it intersects the origin '$O$'. Consider a sub-region of half width '$L$' such that $L < R$. The integrated EELS signal, $M(E)$, for this sub-region contains information from the analysis volume whose projection in the $yz$-plane is represented by ABCD in figure 1. Assuming that the analysis volume has a constant dimension 'λ' along the $x$-axis (this assumption will be discussed in more detail further on), equation (1) reduces to:

$$M(E) = \lambda A_{\text{core}} C(E) + \lambda A_{\text{shell}} S(E) \quad \ldots (2)$$

where $A_{\text{core}}$ and $A_{\text{shell}}$ are the cross-sectional areas of the core and shell regions in the *yz*-plane and within the analysis volume ABCD. From figure (1) it is found that:

$$\begin{aligned} A_{\text{core}} &= 4\int_0^L \sqrt{R^2 - y^2}\, dy \\ &= R^2\left[2\vartheta + \sin(2\vartheta)\right] \end{aligned} \quad \ldots (3)$$

where $\sin(\square) = (L/R)$ and $L < R$. Furthermore:

$$A_{\text{shell}} = 4Rh\vartheta \quad \ldots (4)$$

Equation (4) is simply the perimeter of the core region within the analysis volume ABCD (figure (1)) multiplied by the shell thickness '*h*'. It therefore overestimates the shell area within ABCD but the error can be neglected provided '*h*' is small compared to '*R*'. Substituting equations (3) and (4) in equation (2) and rearranging gives:

$$\frac{M(E)}{4R\vartheta} = \frac{R}{2}\left[1 + \frac{\sin(2\vartheta)}{2\vartheta}\right]\lambda C(E) + h\lambda S(E) \quad \ldots (5)$$

Equation (5) indicates that for a fixed value of '*E*' a plot of $\frac{M(E)}{4R\vartheta}$ vs. $\frac{R}{2}\left[1 + \frac{\sin(2\vartheta)}{2\vartheta}\right]$ is a straight line with gradient proportional to $C(E)$ and intercept proportional to $S(E)$. Data points for the graph at constant energy '*E*' are obtained by varying the half width of the spectrum image sub-region '*L*' over the range $0 < L < R$. Least squares fitting is used to obtain best estimates of the gradient and intercept (see for example [13] for details of least squares fitting). The process is repeated for all values of '*E*' of interest so that the shapes of the pure shell spectrum, $S(E)$, and the pure core spectrum, $C(E)$, are fully extracted.

In deriving equation (5) it was implicitly assumed that the integrated signal extracted from a given sub-region of the spectrum image corresponds precisely to the volume of material enclosed by the sub-region. In practice beam spreading of a STEM probe within the specimen means that this is not always the case. Consider first a parallel-sided thin foil specimen as shown schematically in figure 2(a). The individual columns A, B and C represent the individual pixels of a line spectrum image. A STEM probe incident on column B will have some of its intensity within columns A and C due to beam spreading. The EELS signal measured from pixel B therefore partly contains information from the surrounding material. However, for a sub-region the measured EELS signals from several pixels must be summed to give $M(E)$. Figure 2(a) also shows the beam spreading of a STEM probe incident on column C. By symmetry it is clear that the intensity within

column C for a probe incident on column B is equal to the intensity within column B for the probe incident on column C. For a parallel sided thin foil beam spreading effects are therefore largely 'averaged out' in the integrated signal $M(E)$.

Figure 2(b) is the equivalent diagram for beam spreading in a spherical nanoparticle. Due to the curvature of the nanoparticle, the thickness of a column decreases monotonically with distance from the nanoparticle centre and hence, for a probe incident on an outer column (e.g. column C), beam spreading to the neighbouring columns will be asymmetrical. Beam spreading effects in a spherical nanoparticle will therefore not be 'averaged out' when extracting $M(E)$. There is also a variation in the beam spreading parameter 'λ' (equation (2)), such that λ is greater for a beam positioned at the centre of the nanoparticle compared with a beam at the nanoparticle edge. It should be noted however, that figures 2(a) and 2(b) show the beam finely focused at the specimen entrance surface, although it is strictly an Airy disc. Further beam broadening will only take place once the geometric spreading is equal to the size of the Airy disc. Beam propagation will therefore be 'quasi-cylindrical' in shape about its focal point. For a 10 mrad probe at 200 kV (the conditions used in this paper) a probe focused at the specimen entrance surface must travel a distance of ~15 nm into the particle before further beam spreading can take place. A distance of 15 nm is comparable to the size of the nanoparticles analysed in this paper, so that any beam spreading effects are reduced. In fact, analysis of experimental data below gives physically realistic results and hence the errors seem to cause only a small perturbation of the results.

## 3. Experimental procedure

TiN and Cu nanoparticles were oxidised to produce Ti-oxide and Cu-oxide shell regions respectively. The oxidation conditions were not well controlled. Hence no firm conclusions can be drawn on the oxidation characteristics of these nanoparticles, so that such conclusions are beyond the scope of this paper. The nanoparticles were deposited onto a holey carbon grid and examined in a JEOL 2100F FEG TEM operating at 200 kV in STEM mode with a GIF Tridiem for EELS analysis. The STEM probe semi-convergence angle was 10 mrad. The nanoparticles were characterised in the following sequence: first a 'high resolution' STEM bright field image was acquired at long camera length, from which the core radius '$R$' was estimated. Next the camera length was decreased for spectrum imaging, during which HAADF and EELS signals were collected simultaneously. The short camera length improves the EELS collection efficiency but degrades the STEM image signal-to-noise ratio, which was nevertheless of sufficient quality to observe the outline of the nanoparticle and thereby define a suitable region for spectrum imaging. For spectrum imaging, the EELS collection semi-angle is 30 mrad and the HAADF detector inner angle is 110 mrad. At these large EELS collection angles, there is a stray inelastic signal due to secondary electrons generated at the FEG extraction anode entering the spectrometer [14]. For the experimental conditions used in this study the stray inelastic signal contains a broad 'hump' between 415-600 eV, somewhat similar to the feature reported in [14]. This will introduce artefacts in the N, Ti and O edges if the signal from the specimen is small compared to the stray signal (for example at the edges of the nanoparticle where the specimen thickness is small). Attempts were made to subtract a 'hole spectrum' (i.e. an EELS spectrum acquired with the electron beam positioned over the vacuum) from the raw data prior to applying the analytical method, but this caused artefacts in the processed results, especially for core loss edges with a small number of counts (e.g. the O K-edge in

the TiN core, Ti-oxide shell nanoparticles). Results in this paper are therefore based on unprocessed data, i.e. raw data without a hole spectrum subtracted.

The EELS line spectrum image was acquired at a dispersion of 0.3 eV/channel by scanning the beam in equal steps whose size depends on the particular particle but was typically in the 0.1 to 0.2 nm range. At each spectrum image pixel, the HAADF signal was also simultaneously collected. For non-channeling specimens, the HAADF signal varies linearly with specimen thickness. Hence the projected shape of the nanoparticle can be compared to the ideal spherical geometry using the HAADF trace. This is done by least squares fitting the ideal HAADF trace expected from a spherical nanoparticle to the experimental HAADF data (the fitted trace has the general form $\alpha y^2 = -x^2 + \beta$, where $\alpha$ and $\beta$ are constants to be determined). The spatial drift during EELS acquisition was estimated by comparing the position of the nanoparticle in bright field or HAADF images acquired before and after spectrum imaging and was found to be ~1 nm/min.

EELS core loss edges were background subtracted using a power law fit [12] before being processed according to the method described in section 2. The EELS spectrum varies more rapidly at the edges of a core-shell nanoparticle compared to its centre. Furthermore, in equation (5), the denominator in the ordinate term tends to zero for short sub-regions so that random and systematic errors in $M(E)$ are magnified. Hence a relatively large number of pixels was used for the sub-region with the shortest length. Longer sub-regions were constructed by increasing the number of pixels by a fixed amount until the half-length of the sub-region extended to nearly the radius of the core region. Data from 7 or more sub-regions were therefore used in least squares fitting of the line to equation 5. The sub-regions are symmetrical about the centre of the nanoparticle (figure 1). The 'centre' was defined as the mid-point between the two end positions of the nanoparticle at which the measured HAADF intensity (acquired during spectrum imaging) had decreased to the level of the surrounding vacuum. The optimum fitting parameters (i.e. number of pixels for smallest sub-region and step size of subsequent sub-regions) were established by visually examining the correlation coefficient, $r^2$, for least squares fitting. $r^2$ measures the 'goodness of fit' of the least squares straight line to the data points and has a maximum value of 1 for a perfect fit. It must be noted that '$R$' is the only input parameter in equation (5). The extracted intercept contains '$h$' as a multiplying constant. While this does not affect the shape of the extracted shell spectrum it must be taken into account for quantitative analyses, such as, for example, elemental concentration ratios between core and shell regions.

## 4. Results

### 4.1 *TiN core, Ti-oxide shell nanoparticles*

Figure 3(a) shows the STEM bright field image of a TiN core, Ti-oxide shell nanoparticle. Lattice fringes are partly visible in the outer shell region but not the inner core region, presumably due to the TiN being off zone-axis. The inscribed circle is the estimated boundary of the core region and has a radius of 3.7 nm. The shell region is ~1.5 nm thick. Figure 3(b) is the HAADF line profile of the nanoparticle acquired during EELS spectrum image acquisition (the approximate position of the spectrum image and its scan direction are indicated by the broken, arrowed line in figure 3(a)). The calculated HAADF line profile for an ideal spherical nanoparticle, determined by least squares fitting, is also

superimposed in the figure. The correlation coefficient ($r^2$) for least squares fitting is 0.85 and suggests a significant deviation in the shape of the nanoparticle from ideal spherical geometry. In particular, there is a 'shoulder' (see the arrow in figure 3(b)) observed on the left hand side of the experimental HAADF trace, which suggests a bulge in the nanoparticle shape at that position. In figure 3(c) the integrated EELS signal for the background subtracted N K, Ti $L_{2,3}$ and O K-edges are plotted for each pixel in the spectrum image, along with the simultaneously measured HAADF intensity. For visual comparison, the individual curves have been normalised to a common integrated intensity at the centre of the nanoparticle. There is an overlap between the Ti L-edges (especially the Ti $L_1$-feature) and the O K-edge, which makes background removal, using a power law fit [12], difficult for the latter. The Ti, O profiles have similar widths but are wider than the N profile due to the core-shell nature of the nanoparticle. There is also a 'shoulder' in the Ti profile that overlaps spatially with the 'shoulder' in the HAADF curve (see figure 3(b) for the position of the 'shoulder'). However, the same feature is only weakly observed in the N profile, which suggests that the 'shoulder' is largely caused by a bulge in the oxide shell at that position. The O profile has a plateau region at the centre of the nanoparticle, although, by geometry of the model, the distribution profile for an element confined to the shell region should be a minimum at this position [6]. This is most likely due to the residual Ti signal still present in the 'background subtracted' O K-edge. The difference in width between the Ti and N element distribution profiles is a measure of the shell thickness multiplied by a factor of 2. The Ti-oxide shell thickness is estimated to be 0.6 nm if the 'width' of an element profile is defined as its full width at half maximum (FWHM). This is smaller than the value of 1.5 nm estimated from the STEM bright field image (figure 3(a)). The radius of the TiN core region determined from the FWHM of the N distribution profile is however 3.7 nm, in good agreement with the bright field image estimate.

Before discussing the results of the analytical method we examined the robustness of the technique with respect to two critical parameters: (i) the core radius '*R*' and (ii) the position of the nanoparticle centre. Due to a non-ideal particle geometry there is uncertainty in defining these parameters. To test the importance of '*R*' the core radius was varied by ±0.5 nm from its estimated value (i.e. 3.7 nm, figure 3(a)), while keeping the position of the centre fixed (see section 3 for the method of estimating the centre position). The analytical method is applied to the N K-edge within the energy range 395-450 eV, i.e. least squares fitting is carried out at each energy loss using EELS data extracted from sub-regions of the spectrum image (section 2). Figures 4(a) and 4(b) show results for the extracted gradient and intercept values as a function of energy loss, for $R$ = 3.2, 3.7 and 4.2 nm and fixed centre position. There is a small systematic shift of the curves with increasing '*R*', particularly for the intercept curve (figure 4(b)). The intercept curve is closest to zero for $R$ = 3.7 nm, and since no N is expected in the shell region, this core radius value appears to give the best results. Next the effect of a variation in the centre position of the nanoparticle is explored, while keeping '*R*' fixed at 3.7 nm. The centre is shifted by ±0.5 nm from the position estimated using the experimental HAADF trace (section 3; a positive shift corresponds to moving the centre from left to right along figure 3(b)). The results for the extracted gradient and intercept values, as a function of energy loss, are plotted in figures 4(c) and 4(d) respectively. The curves show only small, systematic changes due to a shift in the centre position. This suggests that, for this particular nanoparticle, the analytical method gives sufficiently robust results.

Results from the analytical method, with $R$ = 3.7 nm and zero shifting of the estimated centre position, are now presented. Figure 5(a) shows the correlation coefficient ($r^2$) for the least squares fit over the 395-450 eV energy range corresponding to the N K-edge. The quality of the fit is poor at energy losses below the edge onset due to the residual noise still remaining after background subtraction. The inset is an enlarged view of $r^2$ above the edge onset (i.e. 405-450 eV). The mean value of $r^2$ within this energy range is 0.98, indicating a linear relationship between the data points. Figure 5(b) is the shape of the N K-edge for the TiN core region extracted from the gradients of the least squares fit straight lines along with standard errors from the fits. The relative standard error is less than 11% which indicates that the extracted N K-edge spectrum is statistically significant. A N K-edge from a TiN standard, published in reference [15], is also shown in figure 5(b) for comparison. This reference spectrum has been shifted along the energy loss axis to align it with the extracted core spectrum. The integrated intensity has been normalised for direct visual comparison. The two spectra share the same gross ELNES features, although there is some difference in the relative intensities between individual peaks. Figure 5(c) shows the N K-edge for the Ti-oxide shell region extracted from the intercepts of the least squares fit straight lines along with the standard error. Throughout this paper the extracted core and shell spectra for a given element are plotted on a common vertical scale for direct visual comparison. The N K-edge intensity is considerably lower in the shell spectrum compared to the core spectrum and the relative standard error for the former has a mean value as large as 247%. These results indicate that any N in the shell region is beyond the detection limit and/or within the error of the analytical extraction method. The lack of any significant N in the shell region is, however, consistent with the larger width of the Ti profile across the nanoparticle compared to that of the N, as observed in figure 3(c).

The analytical method could, in principle, be used to analyse the Ti $L_{2,3}$ and O K-edges along similar lines to the N K-edge. However, the strong overlap of the O K-edge with the Ti $L_{2,3}$-edge means that it is difficult to accurately extract the O K-signal using a power law for the pre-edge background intensity. This is overcome using a two-step process: (i) the analytical method is applied to the background subtracted Ti $L_{2,3}$-edge over an energy loss range large enough to include the O K-edge and (ii) after suitably normalising the Ti $L_{2,3}$-edge, the extracted core spectrum is subtracted from the extracted shell spectrum, leaving only the O K-edge as the residual. The second step is sensitive to any changes in the Ti $L_{2,3}$-near edge fine structure between TiN and Ti-oxide, but its effects can be minimised by using a post-white line (i.e. 480-525 eV) energy window for normalisation.

Figure 6(a) shows the correlation coefficient ($r^2$) for least squares fitting of straight lines within the (Ti $L_{2,3}$ + O K) edge energy loss range of 445-595 eV. The inset is an enlarged view of $r^2$ above the edge onset (i.e. 453-595 eV). At this energy loss range $r^2$ has a mean value of 0.99 which indicates a linear relationship between the data points. Figures 6(b) and 6(c) show the extracted (Ti $L_{2,3}$ + O K) spectra for the core and shell regions respectively along with the standard error. The relative standard error is less than 8% for the core spectrum. The relative standard error over the energy loss range corresponding to the Ti $L_{2,3}$-white lines and the broad peak at ~560 eV in the shell spectrum (figure 6(c)) has a mean value of no more than 27%, so that these spectral features are genuine. In figure 6(d), the extracted core and shell spectra have been superimposed with the integrated intensity in the 480-525 eV energy window normalised. The shell spectrum has a higher normalised intensity above ~530 eV compared to the core spectrum which is consistent with the presence of O in the outer regions of the nanoparticle. The O K-edge in the shell region was

extracted by subtracting the (Ti $L_{2,3}$ + O K) core spectrum (figure 6(b)) from the (Ti $L_{2,3}$ + O K) shell spectrum (figure 6(c)). The extracted O K-edge is shown in figure 6(e). Before subtraction, the integrated intensity within the post-white line energy window of 480-525 eV for the core spectrum was normalised to that of the shell spectrum, so that the O K-edge in figure 6(e) and the Ti $L_{2,3}$-edge in figure 6(c) are plotted on the same intensity scale. The process of normalisation and subtraction of the extracted core spectrum can be carried out at each pixel of the spectrum image to generate a more accurate O distribution profile. The O profile extracted in this way is shown in figure 6(f) along with the Ti and N profiles from figure 3(c). The maximum O intensity has been normalised to the plateau intensity of the Ti and N profiles. In extracting the O distribution, it was observed that the elemental concentration in the vacuum regions outside the nanoparticle did not decay to zero. This is due to the residual stray signal at the O K-edge energies, which was not accurately subtracted by a power law background fit when an energy window preceding the Ti $L_{2,3}$-edge was used to model the background. The residual stray signal gave rise to a constant background on which the 'true' O distribution is superimposed. In figure 6(f) this background has been subtracted for a direct comparison with the Ti and N distributions. The O intensity is zero at the nanoparticle centre due to the nature of the extraction process, although in reality some amount of O is expected. Furthermore the O peak on the left hand side of the particle is more intense and narrower than the right hand side peak and overlaps with the 'shoulder' observed in the Ti profile. This is further evidence for a non-uniform oxide shell. Figure 6(f) illustrates a further application of the analytical method, i.e. extracting the distribution of elements in situations where background subtraction is troublesome due to underlying core loss edges.

The intensity of the Ti $L_{2,3}$-edge in the extracted core spectrum (figure 6(b)) is greater than that of the extracted shell spectrum (figure 6(c)) by a factor of 2.7. In equation (5) the intercept (or equivalently extracted shell spectrum) contains the shell thickness ($h$) as a multiplying factor (the beam spreading parameter 'λ' is common to both the gradient and intercept of the least squares fit straight line and hence, for our purposes, can be ignored). Multiplying the Ti $L_{2,3}$-intensity ratio by $h$ therefore gives the volume density ratio of Ti atoms ($\rho_{Ti}$) for the core region with respect to the shell region. For $h$ = 1.5 nm (i.e. the value estimated from the STEM bright field image, figure 3(a)) $\rho_{Ti}$ is 4.0, while for $h$ = 0.6 nm (i.e. the value estimated from the element distribution profiles, figure 3(c)) $\rho_{Ti}$ is 1.6. These experimental values can be compared with theoretical values calculated from the crystal structure of TiN corresponding to the core region and the appropriate Ti-oxide corresponding to the shell region. There are many forms of Ti-oxide including $TiO_2$ polymorphs as well as the Magnéli phases which have the general formula $Ti_nO_{2n-1}$ [16]. Figure 7(a) shows a region of nanoparticle agglomerate from which the Ti $L_{2,3}$ and O K-edges were acquired in parallel beam mode with an increased dispersion of 0.1 eV/ channel. The background subtracted Ti $L_{2,3}$ and O K-edges are shown in figures 7(b) and 7(c) respectively. The Ti $L_{2,3}$-edge contains contributions from the TiN core and Ti-oxide shell while the O K-edge originates entirely from the Ti-oxide shell. The Ti $L_{2,3}$-white lines (figure 7(b)) and the first major peak 'A' in the O K-edge spectrum (figure 7(c)) do not show evidence for crystal field splitting (the spectrometer energy resolution is 0.8-1.0 eV as measured using the FWHM of the zero loss peak). A comparison of these results with the Ti $L_{2,3}$ and O K-near edge fine structure for the different Ti-oxides published in the literature [16-18] suggests that the Ti-oxide shell region is likely to be a Magnéli phase such as $Ti_3O_5$ but not TiO or $Ti_2O_3$. In TiO the first major peak 'A' of the O K-edge is highly skewed while for $Ti_2O_3$ it shows significant crystal field splitting. For large 'n' the

stoichiometry of the $Ti_nO_{2n-1}$ Magnéli phases approaches that of $TiO_2$ and hence strong crystal field splitting of the Ti $L_{2,3}$ and O K-edges should take place. Note however that the oxide shell region of the nanoparticles may be strained or partially crystallised, with the net result that the broadened spectral features will tend to obscure any crystal field splitting [19]. Evidence for partial crystallisation is indeed visible in figure 3(a). In addition, there is likely to be some beam damage of the Ti-oxide, which would also obscure any crystal field splitting (in fact lattice fringes observed in the Ti-oxide shell of figure 3(a) were not visible along the EELS linescan direction following chemical analysis, indicating beam damage during prolonged exposure). Assuming a TiN core and $Ti_3O_5$ shell with monoclinic crystal structure [20] $\rho_{Ti}$ is calculated to be 1.5. This is similar to the value of 1.6 obtained for $h$ = 0.6 nm (i.e. the EELS determined shell thickness) but not the value of 4.0 obtained for $h$ = 1.5 nm (i.e. the STEM bright field shell thickness). Note however that there is evidence for a non-uniform oxide shell, so that a single value of '$h$' cannot, in principle, be used to derive $\rho_{Ti}$.

The extraction of core and shell spectra for the different elements means that it is possible to calculate the relative element concentrations within a given region (e.g. Ti and O within the Ti-oxide shell). A Hartree-Slater partial cross-section was used for the ionisation probability [12]. The intensity of the extracted spectra was integrated over an energy range sufficiently above the edge onset, away from the near edge fine structure (e.g. Ti $L_{2,3}$-white lines), since Hartree-Slater cross-sections do not accurately model solid state effects or spin-orbit coupling. From the extracted N K-edge core spectrum in figure 5(b) and the extracted Ti $L_{2,3}$-core spectrum in figure 6(b) the N to Ti ratio in the TiN core region was estimated to be 1.3. This is larger than the expected value of 1.0. TiN can form over a wide stoichiometry range [15] but the required conditions (i.e. high energy deposition) are unlikely to have taken place in this particular case. From the extracted Ti $L_{2,3}$-shell spectrum in figure 6(c) and the extracted O K-shell spectrum in figure 6(e) the O to Ti ratio in the shell region is estimated to be 3.6. This is larger than the maximum O to Ti ratio of 2.0 found in $TiO_2$. There are many sources of error that affect the calculated relative element concentrations, such as uncertainties in a standardless Hartree-Slater ionisation cross-section, poor counting statistics of EELS edges as well as accuracy of the analytical method (see section 5 for more details). However, the most serious error is likely to be the stray inelastic signal, since it has already been observed that the O distribution profile in figure 6(f) is superimposed on a constant background. This will increase the O to Ti ratio as observed in the data analysis.

### 4.2 *Cu core, Cu-oxide nanoparticles*

Figure 8(a) shows the STEM bright field image of a Cu core, Cu-oxide nanoparticle with the inscribed circle representing the perimeter of the core region. The approximate position of the spectrum image as well as the scan direction is indicated by the broken, arrowed line in figure 8(a). The core radius, as determined from the bright field image, is ~13.7 nm and the shell thickness is ~1.3 nm. Strong diffraction contrast is observed at the centre of the nanoparticle which may be caused by faceting or an internal grain. Figure 8(b) is the HAADF intensity trace of the nanoparticle acquired during EELS spectrum imaging. The least squares fit HAADF trace for an ideal spherical nanoparticle is superimposed in the figure and has a $r^2$ value of 0.92. The slope of the ideal fit HAADF curve is steeper than the experimental curve, which suggests that the outer edges of the nanoparticle are more 'angular' shaped than spherical. In figure 8(c) the integrated intensity of background

subtracted, O K and Cu $L_{2,3}$-edges are plotted at each pixel along the spectrum image. The maximum intensity of each curve has been normalised for display purposes. At the outer edges of the nanoparticle the O profile is at its peak while the Cu intensity is decreasing, which is consistent with the presence of an oxide shell (the O peak in the right hand side of figure 8(c) contains some signal from the neighbouring nanoparticle; see figure 8(a)). At the centre of the nanoparticle however, the O intensity is close to zero, although in principle some intensity due to the shell region is expected. This is partly due to the strong diffraction contrast observed in this region (figure 8(a)).

Before proceeding with data analysis the robustness of the analytical method was examined with respect to the core radius '*R*' and nanoparticle centre, as described in section 4.1. In particular, '*R*' was varied by ±0.5 nm from the estimated value (i.e. 13.7 nm) while keeping the centre fixed and in a separate test the centre was shifted by ±0.5 nm for $R$ = 13.7 nm. No significant differences in the least squares fit gradient and intercept values were observed for energy losses corresponding to the O K and Cu $L_{2,3}$-edges, suggesting that the extracted spectra were sufficiently robust with respect to the input parameters.

Figure 9(a) plots the correlation coefficient $r^2$ for least squares fitting of straight lines within the O K-edge energy range of 530-600 eV according to the analytical method described in section 2. The mean $r^2$ value at energy losses above the edge onset (i.e. 535-600 eV) is 0.90. The quality of fit is inferior compared to that for the previous data for the TiN core, Ti-oxide nanoparticle. Figures 9(b) and 9(c) show the extracted core and shell spectra for the O K-edge along with their standard errors. (In figure 9(b) the negative standard error is displayed for visual clarity). The relative standard errors in figures 9(b) and 9(c) have a mean value of 12%. Significantly more O is present in the extracted shell spectrum compared to the extracted core spectrum. The latter has negative intensity which is due to the fact that the O profile is negative or close to zero at the nanoparticle centre (figure 9(c)). The presence of an O K-edge in the extracted shell spectrum is consistent with the formation of a Cu-oxide surface layer.

A similar analysis is carried out for the Cu $L_{2,3}$-edge. In figure 10(a) the correlation coefficient for least squares fitting is plotted within the Cu $L_{2,3}$ energy range of 930-1080 eV. The inset is an enlarged view of the curve for energy losses above the edge onset (i.e. 940-1080 eV). The mean value of $r^2$ within this energy range is 0.99. Figures 10(b) and 10(c) show the extracted Cu $L_{2,3}$-spectra for the core and shell regions along with their standard errors. The relative error has a mean value of 2% in figure 10(b) and in figure 10(c) the mean relative error is less than 14% within the energy ranges corresponding to the important spectral features (i.e. 935-940 eV and 960-1020 eV). The intensity of the extracted core spectrum does not decrease even at energies as large as 100 eV above the edge onset. The extracted shell spectrum shows a stronger $L_3$ white line intensity as required for a Cu-oxide [21-22] but there is a sudden decrease in intensity above ~1020 eV. Thus both extracted core and shell spectra do not give the correct edge shapes at high energy losses. It is unclear if the power law fit used to remove the background arising from the specimen and stray inelastic signal is valid at energy losses significantly higher than the edge onset. Furthermore there could be errors in the analytical method, particularly due to a non-spherical particle shape (figure 8(a)), although it is not clear why the error would vary with energy loss above the edge onset.

In figure 10(d) the extracted Cu $L_{2,3}$-core and shell spectra are superimposed and their integrated intensities within a 930-1000 eV energy window normalised for direct visual comparison. The edge onset energies for the two curves are similar. Furthermore the $L_3$ white line in the shell spectrum is slightly asymmetric, i.e. it has a broader high energy 'tail'. These observations are consistent with a $Cu_2O$ spectrum rather than CuO (for the latter the $L_3$ white line is symmetrical and there is a ~2.5 eV chemical shift to lower energy loss with respect to pure Cu [21-22]). From the relative intensities of the extracted Cu $L_{2,3}$-core and shell spectra it is possible to calculate the volume density ratio ($\rho_{Cu}$) of Cu atoms in the core region with respect to the shell region along the lines described in section 4.1. For $h$ = 1.3 nm (i.e. shell thickness estimated from the STEM bright field image, figure 8(a)) the experimental value of $\rho_{Cu}$ is 0.5. The calculated value for $\rho_{Cu}$, assuming a Cu core and $Cu_2O$ shell, is however 1.6 and is considerably larger than the experimental value (note that a shell of CuO gives a $\rho_{Cu}$ value of 1.7). Assuming the uncertainty in $h$ = 1.3 nm is no more than ±0.5 nm, the experimental value for $\rho_{Cu}$ should be within the range 0.3-0.7, still clearly less than the theoretical value of 1.6. The error in $\rho_{Cu}$ is therefore not entirely due to uncertainties in '$h$', but may also reflect other sources of error in the algorithm.

From the extracted O K-shell spectrum in figure 9(c) and the extracted Cu $L_{2,3}$-shell spectrum in figure 10(c) it is possible to determine the O to Cu ratio in the Cu-oxide shell region. The calculated value, using Hartree-Slater cross-sections, is 2.0 and is larger than the value of 0.5 expected for a $Cu_2O$ shell or the value of 1.0 for a CuO shell. Several sources of error were identified in section 4.1 and these are also applicable for the Cu core, Cu-oxide shell nanoparticles. In the present case the effect of diffraction contrast on the relative element concentration must also be considered. The O concentration is negative or close to zero at the nanoparticle centre (figure 8(c)) and as a result the extracted O K-core spectrum is negative (figure 9(b)) due to a larger intensity being incorrectly assigned to the extracted O K-shell spectrum (figure 9(c)). The extracted Cu $L_{2,3}$-edges are similarly affected although the error involved must be somewhat smaller due to a larger characteristic scattering angle for the higher energy Cu $L_{2,3}$-edge [12]. Taking ratios between the O K and Cu $L_{2,3}$-edge intensities will therefore largely remove any diffraction contrast artefacts from the relative element concentrations.

The extracted Cu $L_{2,3}$-core and shell spectra can be used as reference spectra for MLLS analysis of the spectrum image, i.e. the measured Cu $L_{2,3}$-edge at each pixel in the spectrum image is modelled as a linear combination of the extracted core and shell spectra. The integrated intensity within the 930-1000 eV energy range was normalised, so that the MLLS fit coefficients are proportional to the molar fraction of each phase within the analysis volume. Figure 11 shows the MLLS fit coefficients for the extracted core and shell spectra at each pixel in the spectrum image (MLLS fitting was carried out over the energy range 933-993 eV). Examination of the residual signal did not reveal any significant, systematic intensity, which suggests that the raw data can be successfully modelled using a linear combination of the reference spectra. The fit coefficient for the core spectrum decreases monotonically with distance from the nanoparticle centre while that for the shell spectrum is at its minimum at the centre but peaks further away. The peaks for the shell spectrum profile are broader than that expected for a ~1.3 nm thick shell. The FWHM of Gaussian curves fitted to the peaks on the left and right hand side of the shell profile in figure 11 were 14.4 and 12.4 nm respectively. Beam spreading alone cannot account for the broad peaks, so that the 'angular' shape of the nanoparticle, as deduced from the HAADF curves in figure 8(b), must also have an important effect. In order to check the numerical

accuracy of MLLS fitting it is noted that the ratio of MLLS fit coefficient for the shell spectrum to that of the core spectrum at the centre of the nanoparticle, assuming negligible beam spreading, is approximately $h/(R\rho_{Cu})$. From figure 11 this ratio is measured to be 0.17. For $h$ = 1.3 nm, $R$ = 13.7 nm (figure 8(a)) and $\rho_{Cu}$ = 0.5 (derived from the analytical method) the calculated ratio is $h/(R\rho_{Cu})$ = 0.19 and is in good agreement with figure 11. However, if the theoretical value of $\rho_{Cu}$ = 1.6 (i.e. Cu core and $Cu_2O$ shell) is substituted then $h/(R\rho_{Cu})$ = 0.06 which is considerably smaller than the experimentally derived ratio.

## 5. Discussion

Application of the analytical method to TiN core, Ti-oxide shell and Cu core, Cu-oxide shell nanoparticles has been shown to produce qualitatively consistent results. However, in several cases, such as, for example, the relative element concentrations within the core or shell region or between core and shell regions, the extracted results are found to be quantitatively inaccurate. There are many reasons for the breakdown of the assumptions used in deriving Eq. (5). These include a non-uniform shell thickness, beam spreading as well as multiple scattering and diffraction contrast effects due to the changing thickness across the nanoparticle. Diffraction contrast modifies the total signal entering the EELS spectrometer, while in Eq. (5) perfect collection efficiency is assumed. This will cause the points used to plot Eq. (5) to have additional variability. Multiple scattering causes a redistribution of intensity in the core loss edge. The raw data can be corrected for multiple scattering and diffraction contrast by near-simultaneously acquiring the low loss region of the EELS spectrum using, for example, a dual-EELS system ([23]; see also [10] for more details). A major source of error however, is the assumption of an idealised spherical geometry for the nanoparticle. When the analytical method was first developed for a rough interface [10] the irregular interfacial geometry was directly taken into account by using the HAADF intensity trace acquired across the interface. This requires as input parameters the HAADF intensity for the 'bulk' phases either side of the interface. Furthermore the 'bulk' phases must have identical thicknesses, although a dual-EELS based method for dealing with non-uniform thicknesses was outlined in [10]. These criteria are satisfied for a parallel sided thin foil with the interface in an 'end-on' orientation, but are not applicable for a core-shell nanoparticle where the thickness varies across the nanoparticle and where the beam generally samples a mixture of the core and shell regions rather than the pure 'bulk' phase(s). Errors due to an irregular nanoparticle geometry are therefore unavoidable and must be taken into account to approach a fully quantitative interpretation.

Consider, for example, an ellipsoidal shaped core-shell nanoparticle. The nanoparticle cross-section, through which the spectrum image is acquired, has the shape of an ellipse with semi-major axis ($a$) parallel to the spectrum imaging direction (i.e. the $y$-axis) and the semi-minor axis ($b$) parallel to the electron optic axis (i.e. the $z$-axis, see figure 12(a)). Sub-regions of half length '$L$', corresponding to the analysis region 'ABCD' in figure 12(a), are extracted from the parent spectrum image. The cross-sectional area for the core region ($A'_{core}$) within the sub-region of half length '$L$' is given by:

$$A'_{core} = 4\int_0^L z\,dy$$

$$= 2ab\left[\arcsin\left(\frac{L}{a}\right)+\left(\frac{L}{a}\right)\sqrt{1-\left(\frac{L}{a}\right)^2}\right]$$

... (6)

where the equation for an ellipse, i.e. $(y/a)^2 + (z/b)^2 = 1$, was used in the derivation. The cross-sectional area of shell material ($A'_{shell}$) within the sub-region of half length '$L$' is approximately:

$$A'_{shell} = 4h\int_0^L \sqrt{1+\left(\frac{dz}{dy}\right)^2}\,dy$$
$$= 4ah\int_0^{\arcsin\left(\frac{L}{a}\right)} \sqrt{1-e^2\sin^2\theta}\,d\theta = 4ahE\left[\arcsin\left(\frac{L}{a}\right);e\right]$$

... (7)

where the eccentricity ($e$) is defined as, $e^2 = 1-(b/a)^2$. The integral $E[\arcsin(L/a);e]$ is an incomplete elliptic integral of the second kind and has no analytical solution. Equation (7) overestimates the shell area in a similar way to equation (4). Consider approximating the ellipsoidal nanoparticle to a sphere of average radius, $R_{avg} = (a + b)/2$, and applying equation (5) to extract the core and shell spectrum. This is similar to the experimental situation, since in reality the shape of the nanoparticle is likely to deviate from that of a sphere. A sub-region of half length '$L$' would therefore be assumed to have a core area given by $A_{core}$ (equation (3), with $R_{avg}$ replacing $R$) although the true area is $A'_{core}$ (equation (6)), and similarly for the shell region (equations (4) and (7)). The effect of this approximation on the numerical accuracy is investigated using the parameter ($f_{core}/f_{shell}$), where:

$$f_{core} = A_{core} / A'_{core}$$
$$= \frac{\left[1+\sqrt{1-e^2}\right]^2}{4\sqrt{1-e^2}} \cdot \frac{\left[\arcsin\left(\frac{2L/a}{1+\sqrt{1-e^2}}\right)+\left(\frac{2L/a}{1+\sqrt{1-e^2}}\right)\sqrt{1-\left(\frac{2L/a}{1+\sqrt{1-e^2}}\right)^2}\right]}{\left[\arcsin(L/a)+(L/a)\sqrt{1-(L/a)^2}\right]}$$
$$f_{shell} = A_{shell} / A'_{shell}$$
$$= \left[\left(1+\sqrt{1-e^2}\right)\arcsin\left(\frac{2L/a}{1+\sqrt{1-e^2}}\right)\right] \Big/ 2E\left[\arcsin(L/a);e\right]$$

... (8)

For a given eccentricity ($f_{core}/f_{shell}$) depends only on ($L/a$). ($f_{core}/f_{shell}$) = ($A_{core}/A_{shell}$)/($A'_{core}/A'_{shell}$), compares the estimated core to shell area fraction to the true value. Figure 12(b) is a plot of ($f_{core}/f_{shell}$) as a function of ($L/a$) for nanoparticles that have a semi-major to semi-minor axis ratio ($a/b$) of 1.01, 1.05 and 1.10 respectively (the ratios correspond to a 1%, 5% and 10% deviation of the nanoparticle from ideal spherical geometry). For $(L/a) < 0.75$ there is a bias towards the volume of core material, while for $(L/a) > 0.75$ the bias is towards the volume of shell material. Equation (2), from which equation (5) is subsequently derived, requires accurate values for the core and shell areas, in order to decouple $C(E)$ and $S(E)$ from $M(E)$. The biasing observed in figure 12(b) for an

ellipsoidal nanoparticle implies that the analytical method does not decouple the signals from the core and shell regions accurately, so that the shape of the extracted $S(E)$ spectrum contains ELNES features from the shell as well as core region, and similarly for the extracted $C(E)$ spectrum. Furthermore the deviation of $(f_{core}/f_{shell})$ from the ideal value of unity is asymmetrical, i.e. the deviation is larger for $(L/a) > 0.75$ compared to $(L/a) < 0.75$. Hence apart from the shape of the extracted spectra, the analytical method could also be inaccurate with respect to the relative intensities of elements present in the core and shell regions.

It is also of interest to explore the detection limits of the analytical method for the idealised case of a spherical nanoparticle. Two extreme examples would be detecting the modified near edge structure due to changes in the atomic coordination at the surface of a chemically homogeneous nanoparticle and detecting surface adsorption, for example in catalysts [24-25]. In such cases, it is nearly impossible to define the core and shell regions using (for example) conventional STEM bright field imaging, so that the error ($\delta R$) in the estimated core radius is at least of the same magnitude as the shell thickness $h$. Consider the effect of the error $\delta R$ on the extracted shell spectrum $S(E)$. In equation (5) when $\sin(\vartheta) (=L/R) \rightarrow 0$ the abscissa value tends to $R$ and the ordinate tends to $M(E)/(4L)$. Hence for small $L$ the ordinate value is independent of the core radius $R$ and therefore acts as a 'pivoting point' for the least squares fit straight line. For $\sin(\vartheta) = 1$, the abscissa value is $R/2$ and the ordinate value is $\Sigma M(E)/(2\pi R)$, where $\Sigma M(E)$ denotes the integrated EELS signal measured from the entire nanoparticle. The ordinate value for large $L$ is therefore dependent on $R$ and has an error $\Sigma M(E)[\delta R/2\pi R^2]$. As illustrated schematically in figure 13, this introduces an error $\Delta\theta$ in the gradient so that, by geometry, the error for the intercept, or equivalently the shell spectrum, is $\Sigma M(E)[\delta R/\pi R^2]$. The relative error, with respect to the true intercept $\lambda h S(E)$, is therefore $(\Sigma M(E)/\lambda h S(E))[\delta R/\pi R^2]$. For the case of an element being present in both the core and shell regions it is reasonable to assume that $\Sigma M(E)$ originates largely from the core and hence $\Sigma M(E) \approx \pi R^2 \lambda C(E)$. The relative error is therefore $(\delta R/h)[C(E)/S(E)]$. The two terms $(\delta R/h)$ and $[C(E)/S(E)]$ are of the same order of magnitude as unity and hence there is a considerable error in extracting the shell spectrum. It is therefore not possible to detect any changes to the near edge fine structure at the surface of a chemically homogeneous nanoparticle using this method. If the element is only present at the surface then $\Sigma M(E) = 2\pi R h \lambda S(E)$ and the relative error is $2(\delta R/R)$. Hence the shell spectrum can be extracted to any arbitrary accuracy provided that the core radius $R$ is suitably large. Furthermore, since the element is not present in the core region, the true gradient of the least squares fit straight line is zero and hence from figure 13 the error in the extracted core spectrum is given by $\Delta\theta = 2\lambda h S(E)[\delta R/R^2]$, which can also be made arbitrarily small for large $R$. For very large $R$ the surface is effectively a plane parallel to the electron beam, and therefore has the ideal geometry for measuring surface chemistry. In principle the analytical method is therefore capable of characterising surface adsorption provided the nanoparticle is sufficiently large, although in reality signal-to-noise ratio in the EELS spectrum will be the limiting factor in such experiments.

## 6. Summary and conclusions

An analytical method has been developed for extracting the core and shell spectra from a core-shell nanoparticle by analysing the EELS signal within sub-regions of varying length obtained from a parent spectrum image. Compared with other techniques such as, for

example, multiple linear least squares fitting, reference spectra from external materials standards are not required. The technique was applied to TiN core, Ti-oxide shell and Cu core, Cu-oxide shell nanoparticles. The extracted core and shell spectra showed the correct distribution of elements within each region. However, the relative concentrations of elements within a given region (e.g. Ti and O or Cu and O in the shell regions) were quantitatively inaccurate. Changes in the EELS near edge fine structure due to variations in atomic coordination between core and shell regions were also reproduced by the analytical method. This is seen in, for example, the Cu $L_{2,3}$-edge for the Cu core, Cu-oxide shell nanoparticle. The extracted Cu $L_{2,3}$-core and shell spectra were used as the reference spectra for MLLS fitting of the raw data in the spectrum image acquired across the nanoparticle. This is an important application of the technique since it eliminates the need for external standards in data modelling.

The analytical method assumes the nanoparticle to be of ideal spherical geometry, although in reality this is rarely the case. The significance of this approximation was investigated by comparing the geometry of an ellipsoidal nanoparticle to that of the assumed spherical shape. The net effect of the approximation is that perfect decoupling of the core and shell spectra is not achieved, i.e. the extracted core spectrum will be a mixture of the true core and true shell spectra and similarly for the extracted shell spectrum. Furthermore, the relative concentration for an element present in both the core and shell regions is likely to be inaccurate. The analytical method is therefore likely to be most useful in qualitative analysis of raw data rather than in any quantitative analyses. Detection limits of the analytical method were also explored for the case of an ideal spherical nanoparticle. The technique is in principle capable of determining if a trace element is localised at the surface, provided the nanoparticle radius is suitably large, although in practice the limiting factor in such experiments will be the signal to noise ratio of the measured EELS spectra. However, extension of the method to detect any changes to the EELS near edge fine structure of surface atoms in a chemically homogeneous nanoparticle is not possible.

## 7. Acknowledgements

BGM would like to thank the Department of Physics, Durham University for providing access to laboratory facilities. AJC would like to thank EPSRC for funding under grant EP/D040205/1

## 8. References

[1] N. Braidy, S. Behal, A. Adronov, G. A. Botton, *Micron*, **39** (2008) 717.
[2] B. Rodriguez- Gonzalez, A. Burrows, M. Watanabe, C. J. Kiely, L. M. L. Marzan, *J. Mater. Chem.*, **15** (2005) 1755.
[3] S. J. Rosenthal, J. McBride, S. J. Pennycook, L. C. Feldman, *Surf. Sci. Reports*, **62** (2007) 111.
[4] C. Wang, D. R. Baer, J. E. Amonette, M. H. Engelhard, J. Antony, Y. Qiang, *J. Am. Chem. Soc.*, **131** (2009) 8824.

[5] A. S. Eggeman, P. J. Dobson, A. K. Petford-Long, *J. Appl. Phys.*, **101** (2007) 024307.
[6] J. Thomas, T. Gemming, *Appl. Surf. Sci.*, **252** (2005) 245.
[7] M. MacKenzie, A. J. Craven, D. A. Hamilton, D. W. McComb, *Appl. Phys. Lett*., **88** (2006) 022108.
[8] M. MacKenzie, A. J. Craven, D. W. McComb, S. De Gendt, *Appl. Phys. Lett.*, **88** (2006) 192112.
[9] D. A. Muller, T. Sorsch, S. Moccio, F. H. Baumann, K. Evans-Lutterodt, G. Timp, *Nature*, **399** (1999) 758.
[10] B. G. Mendis, M. MacKenzie, A. J. Craven, *Ultramicroscopy*, **110** (2010) 105.
[11] C. Jeanguillame, C. Colliex, *Ultramicroscopy* **28** (1989) 252.
[12] R. F. Egerton, *Electron Energy-Loss Spectroscopy in the Electron Microscope*, 2nd edition, Plenum Press, New York, 1996.
[13] G. L. Squires, *Practical Physics*, McGraw-Hill, London, 1968.
[14] D. W. McComb, G. C. Weatherly, *Ultramicroscopy* **68** (1997) 61.
[15] A. J. Craven, *J. Microsc.* **180** (1995) 250.
[16] E. Stoyanov, F. Langenhorst, G. Steinle-Neumann, *Am. Mineralogist*, **92** (2007) 577.
[17] R. Brydson, H. Sauer, W. Engel, J. M. Thomas, E. Zeitler, N. Kosugi, H. Kuroda, *J. Phys.: Condens. Matter*, **1** (1989) 797.
[18] R. Brydson, H. Sauer, W. Engel, F. Hofer, *J. Phys. : Condens. Matter*, **4** (1992) 3429.
[19] T. Manoubi, PhD thesis, Universite de Paris-sud, 1989.
[20] S. Åsbrink, A. Magnéli, *Acta Cryst.*, **12** (1959) 575.
[21] M. Grioni, J. F. van Acker, M. T. Czyzyk, J. C. Fuggle, *Phys. Rev. B*, **45** (1992) 3309.
[22] L. Laffont, M. Y. Wu, F. Chevallier, P. Poizot, M. Morcrette, J. M. Tarascon**,** *Micron*, **37** (2006) 459.
[23] J. Scott, P. J. Thomas, M. MacKenzie, S. McFadzean, J. Wilbrink, A. J. Craven, W. A. P. Nicholson, *Ultramicroscopy* **108** (2008) 1586.
[24] P. D. Nellist, S. J. Pennycook, *Science* **274** (1996) 413.
[25] M. D. Shannon, C. M. Lok, J. L. Casci, *J. Catalysis* **249** (2007) 41.

**Figure captions**

**Figure 1**: Schematic of a spherical core-shell nanoparticle of core radius '*R*' and uniform shell thickness '*h*'. The nanoparticle origin is at the point '*O*'. The line spectrum image is acquired along the *y*-axis and the electron optic axis is parallel to the *z*-axis. See text for further details.

**Figure 2**: Schematic of the beam spreading within (a) a parallel sided thin foil and (b) a spherical nanoparticle. The columns A, B and C represent the individual pixels in a spectrum image. The shading in the beam profile is based on the local electron current density, with darker shades of grey representing a higher current density. See text for further details.

**Figure 3**: (a) STEM bright field image of a TiN core, Ti-oxide shell nanoparticle. The inscribed circle represents the core region and the broken, arrowed line represents the approximate position and scan direction of the line spectrum image. (b) shows the HAADF intensity trace acquired across the nanoparticle simultaneously during spectrum imaging. A least squares fit curve, based on the projected geometry of a sphere, is also superimposed. The arrow indicates the location of a possible bulge in the nanoparticle shape. (c) is a plot of the distribution of N, Ti and O across the nanoparticle derived from the integrated intensities of background subtracted EELS edges. The experimental HAADF curve in (b) is also superimposed. The individual curves have been normalised to a common integrated intensity at the centre of the nanoparticle in order to aid visual comparison.

**Figure 4**: (a) and (b) respectively show the effect of the core radius '*R*' on the extracted gradient and intercept values over an energy loss range corresponding to the N K-edge. The centre of the nanoparticle was kept fixed. (c) and (d) are extracted gradients and intercepts for $R = 3.7$ nm, but where the centre was shifted by ±0.5 nm. See text for further details.

**Figure 5**: (a) shows the correlation coefficient, $r^2$, for least squares fitting of straight lines along the lines of the analytical method within the N K-edge energy loss range. The inset is an enlarged view of $r^2$ at energy losses above the edge onset. (b) and (c) show the extracted core and shell spectra for the N K-edge along with their standard errors. In (b) a N K reference spectrum from TiN, previously published in [15], is also superimposed. The reference spectrum has been shifted along the energy loss axis to align it with the extracted core spectrum and the integrated intensity has also been normalised for a direct comparison.

**Figure 6**: (a) shows the correlation coefficient, $r^2$, for least squares fitting of straight lines along the lines of the analytical method within the (Ti $L_{2,3}$ + O K) edge energy loss range. The inset is an enlarged view of $r^2$ at energy losses above the edge onset. (b) and (c) show the extracted core and shell spectra for the (Ti $L_{2,3}$ + O K) edge along with their standard errors. In (d) the extracted core and shell spectra are superimposed and the integrated intensity within the 480-525 eV energy window normalised for a more direct visual comparison. By subtracting the (normalised) extracted core spectrum from the extracted shell spectrum the O K-edge in the shell region is obtained and is shown in (e). The extracted core spectrum can also be used to obtain a more accurate O distribution profile across the nanoparticle. The O profile thus extracted is shown superimposed in (f) along with the N and Ti profiles from figure 3(b). The maximum intensity of the O profile is normalised to the plateau intensity of the N and Ti profiles for visual clarity.

**Figure 7**: (a) shows an agglomerate of TiN core, Ti-oxide shell nanoparticles from which EELS spectra were acquired in parallel beam mode. The resulting Ti $L_{2,3}$ and O K-edges are shown in (b) and (c) respectively.

**Figure 8**: (a) STEM bright field image of a Cu core, Cu-oxide shell nanoparticle. The inscribed circle represents the core region and the broken, arrowed line represents the approximate position and scan direction of the line spectrum image. (b) shows the HAADF intensity trace acquired across the nanoparticle simultaneously during spectrum imaging. A least squares fit curve, based on the projected geometry of a sphere, is also superimposed. (c) is a plot of the distribution of Cu and O across the nanoparticle derived from the

integrated intensities of background subtracted EELS edges. The maximum intensity of each curve has been normalised in order to aid visual comparison.

**Figure 9**: (a) shows the correlation coefficient, $r^2$, for least squares fitting of straight lines along the lines of the analytical method within the O K-edge energy loss range. (b) and (c) show the extracted core and shell spectra for the O K-edge along with their standard errors. In (b) the negative standard error is plotted in order to aid visual comparison with the extracted core spectrum.

**Figure 9**: (a) shows the correlation coefficient, $r^2$, for least squares fitting of straight lines along the lines of the analytical method within the Cu $L_{2,3}$-edge energy loss range. The inset is an enlarged view of $r^2$ at energy losses above the edge onset. (b) and (c) show the extracted core and shell spectra for the Cu $L_{2,3}$-edge along with their standard errors. In (d) the extracted core and shell spectra are superimposed and the integrated intensity within the 930-1000 eV energy window normalised for a more direct visual comparison.

**Figure 10**: MLLS analysis of the Cu $L_{2,3}$-edge for each pixel of the spectrum image acquired across the Cu core, Cu-oxide shell nanoparticle. The extracted Cu $L_{2,3}$-core and shell spectra were used as the reference spectra for MLLS fitting. The MLLS fit coefficient for each reference spectrum is plotted as a function of position across the nanoparticle.

**Figure 12**: (a) schematic of an ellipsoidal core-shell nanoparticle of uniform shell thickness '*h*'. The core region has a semi-major axis of length '*a*' and a semi-minor axis of length '*b*'. The nanoparticle origin is at the point '*O*'. The line spectrum image is acquired along the *y*-axis and the electron optic axis is parallel to the *z*-axis. (b) shows the variation of $(f_{core}/f_{shell})$ as a function of $(L/a)$ for ellipsoidal nanoparticles of different $(a/b)$ ratios. See text for further details.

**Figure 13**: Effect of an error $\delta R$ in the estimated core radius on the extracted core and shell spectra. The abscissa and ordinate in the figure correspond to equation (5) and represent the axes of the least squares fit straight line from which the core and shell spectra are extracted. The dark line represents the true straight line for the nanoparticle in the absence of any errors while the grey line represents the straight line constructed in the presence of an error $\delta R$ in the estimated core radius. In the analysis data points are only available for abscissa values between $R/2$ and $R$, where $R$ is the true core radius. For visual purposes the straight line is shown to be continuous within this region. To extract the shell spectrum (via the intercept) the straight line must be extrapolated towards the vertical axis and this is indicated by the broken lines which are an extension to the above mentioned solid lines. See text for further details.

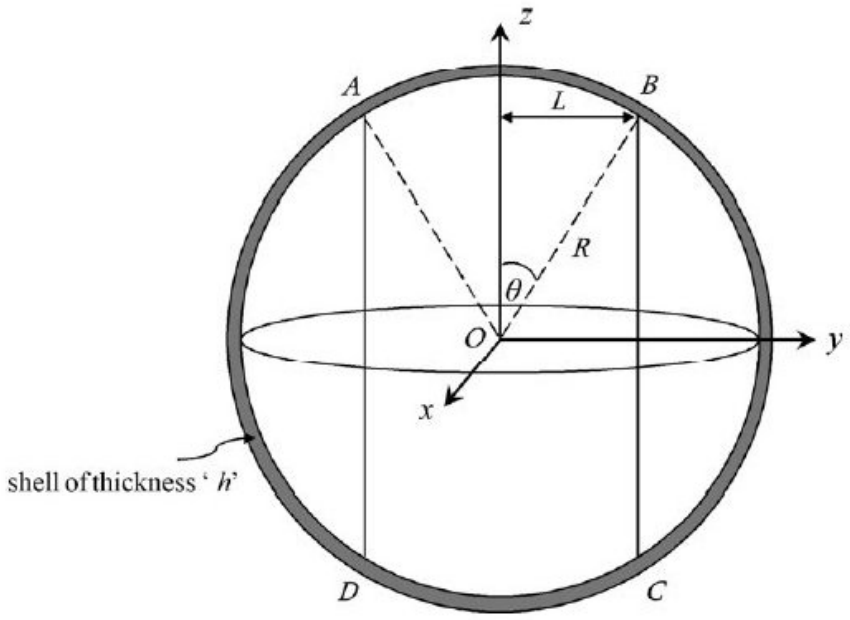


Figure 1

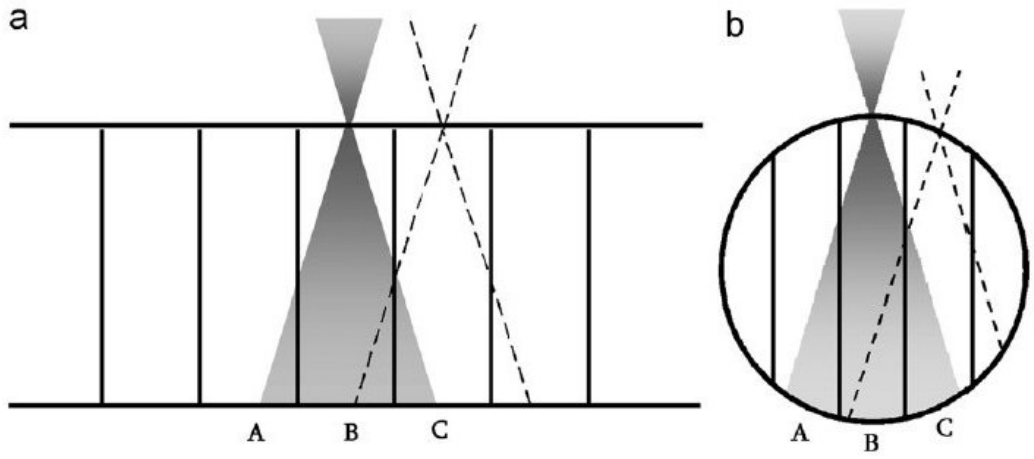


Figure 2

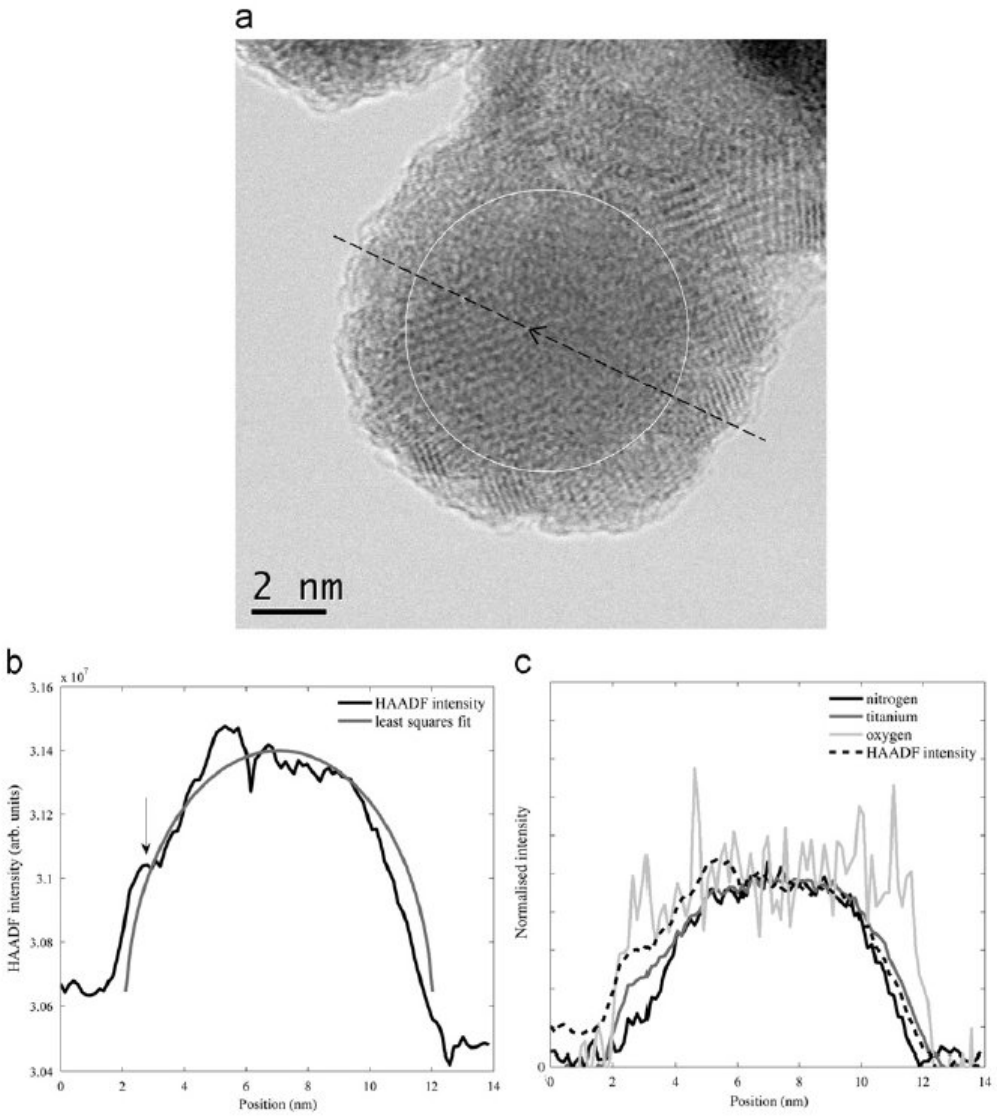
a
2 nm
b
x 10^7
HAADF intensity
least squares fit
HAADF intensity (arb. units)
Position (nm)
c
nitrogen
titanium
oxygen
HAADF intensity
Normalised intensity
Position (nm)

Figure 3

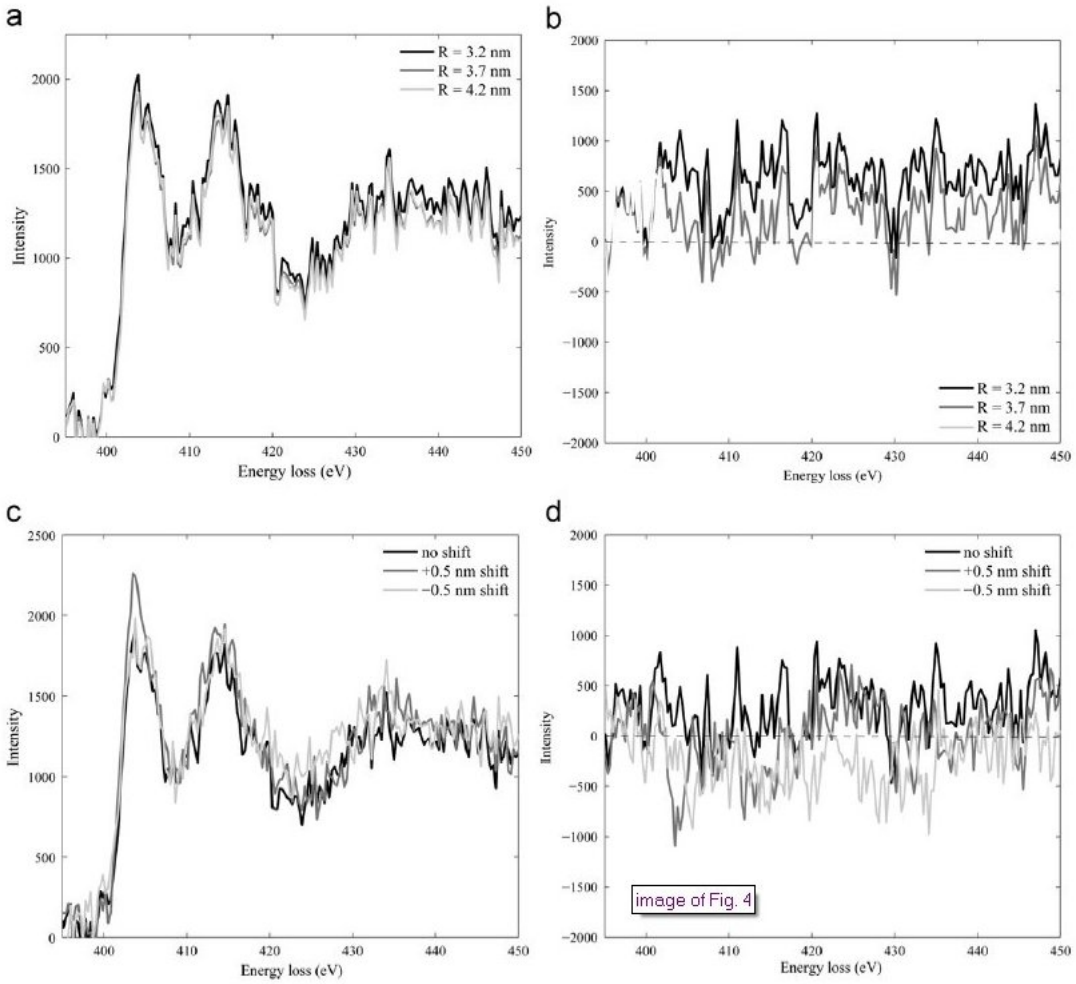
a
R = 3.2 nm
R = 3.7 nm
R = 4.2 nm
Intensity
Energy loss (eV)
b
R = 3.2 nm
R = 3.7 nm
R = 4.2 nm
Intensity
Energy loss (eV)
c
no shift
+0.5 nm shift
−0.5 nm shift
Intensity
Energy loss (eV)
d
no shift
+0.5 nm shift
−0.5 nm shift
image of Fig. 4
Intensity
Energy loss (eV)

Figure 4

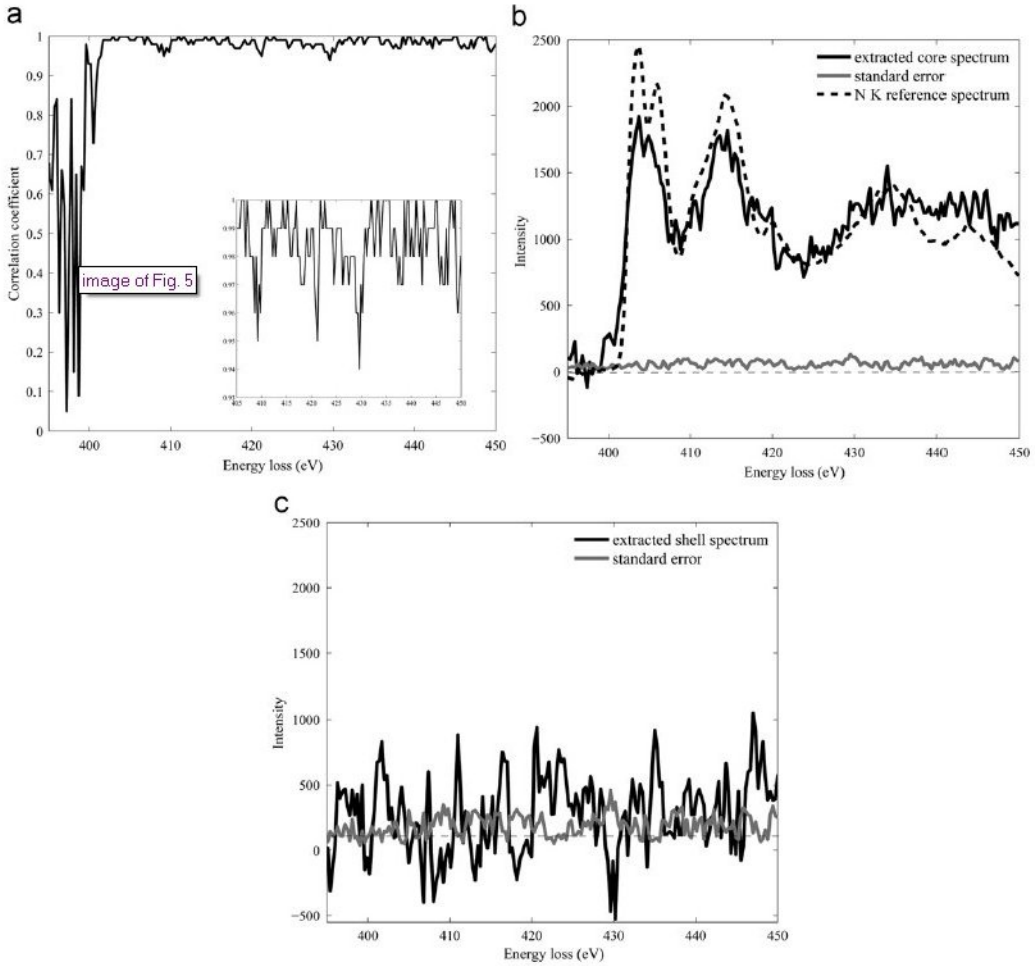
a
Correlation coefficient
Energy loss (eV)
image of Fig. 5
b
extracted core spectrum
standard error
N K reference spectrum
Intensity
Energy loss (eV)
c
extracted shell spectrum
standard error
Intensity
Energy loss (eV)

Figure 5

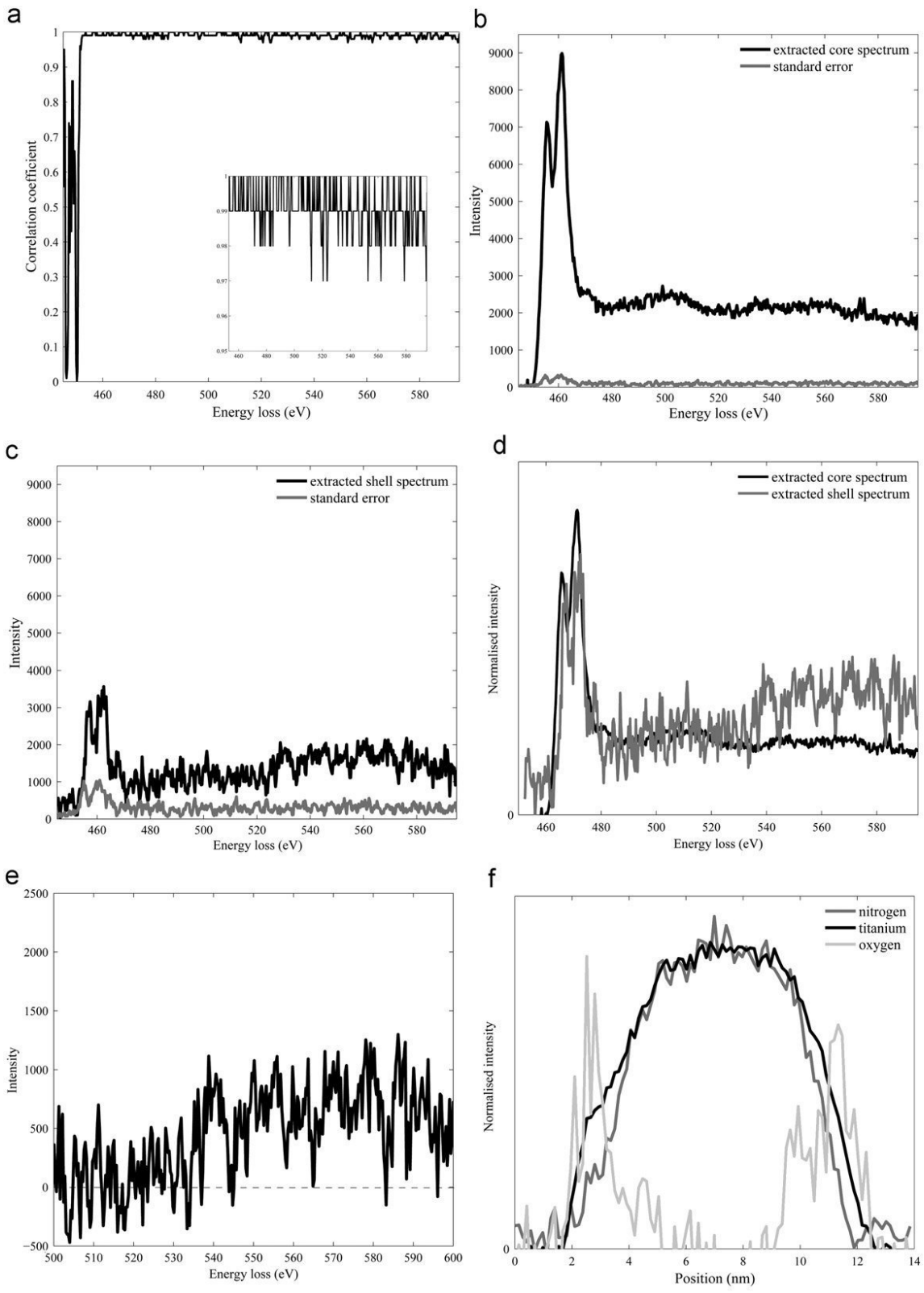
a
Correlation coefficient
Energy loss (eV)
b
extracted core spectrum
standard error
Intensity
Energy loss (eV)
c
extracted shell spectrum
standard error
Intensity
Energy loss (eV)
d
extracted core spectrum
extracted shell spectrum
Normalised intensity
Energy loss (eV)
e
Intensity
Energy loss (eV)
f
nitrogen
titanium
oxygen
Normalised intensity
Position (nm)

Figure 6

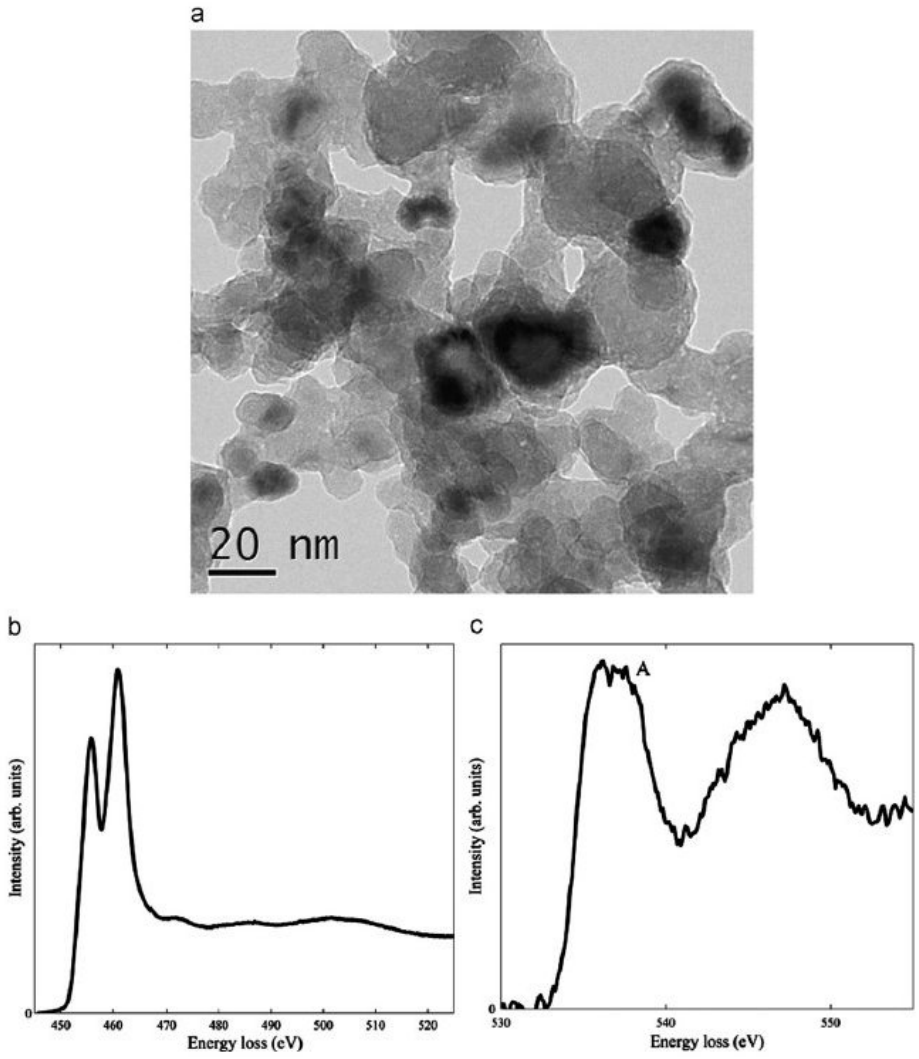
a
20 nm
b
Intensity (arb. units)
0
450
460
470
480
490
500
510
520
Energy loss (eV)
c
A
Intensity (arb. units)
0
530
540
550
Energy loss (eV)

Figure 7

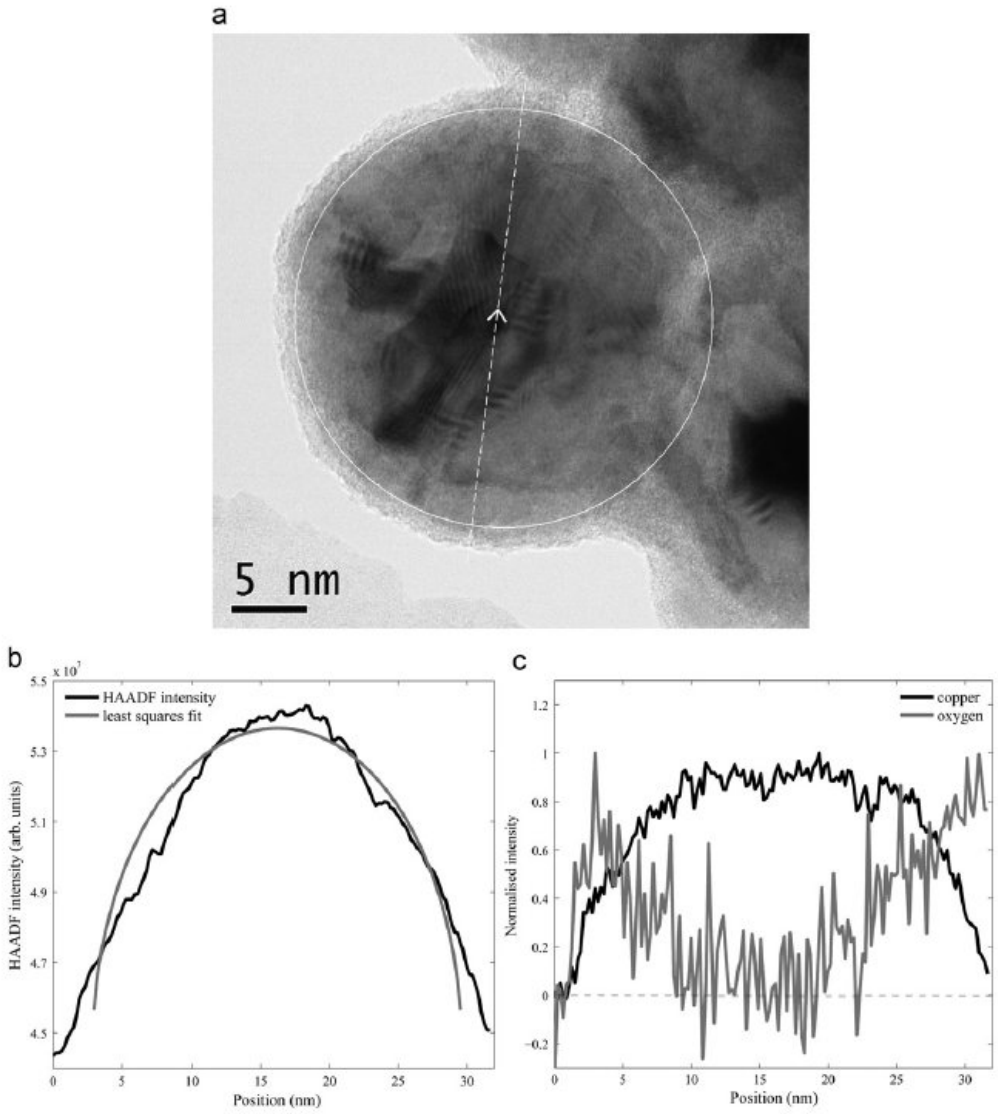
a
5 nm
b
x 10^7
HAADF intensity
least squares fit
HAADF intensity (arb. units)
Position (nm)
c
copper
oxygen
Normalised intensity
Position (nm)

Figure 8

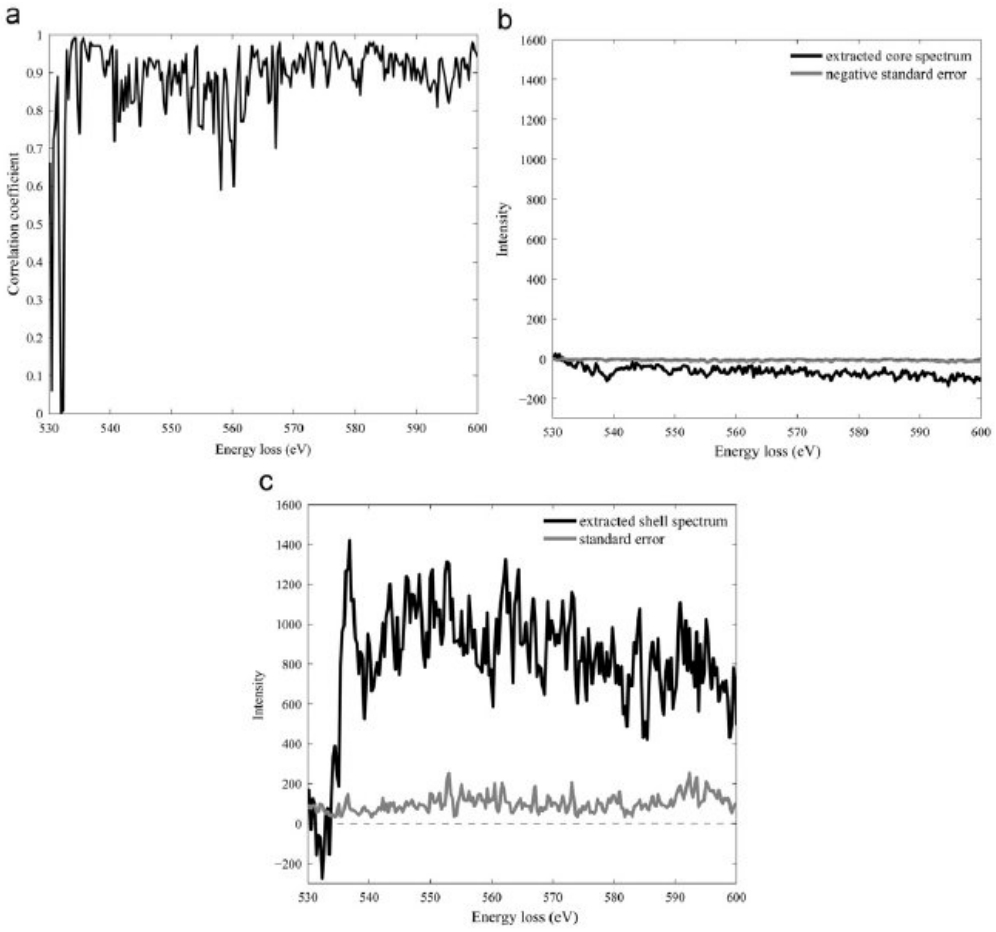
a
Correlation coefficient
Energy loss (eV)
b
extracted core spectrum
negative standard error
Intensity
Energy loss (eV)
c
extracted shell spectrum
standard error
Intensity
Energy loss (eV)

Figure 9

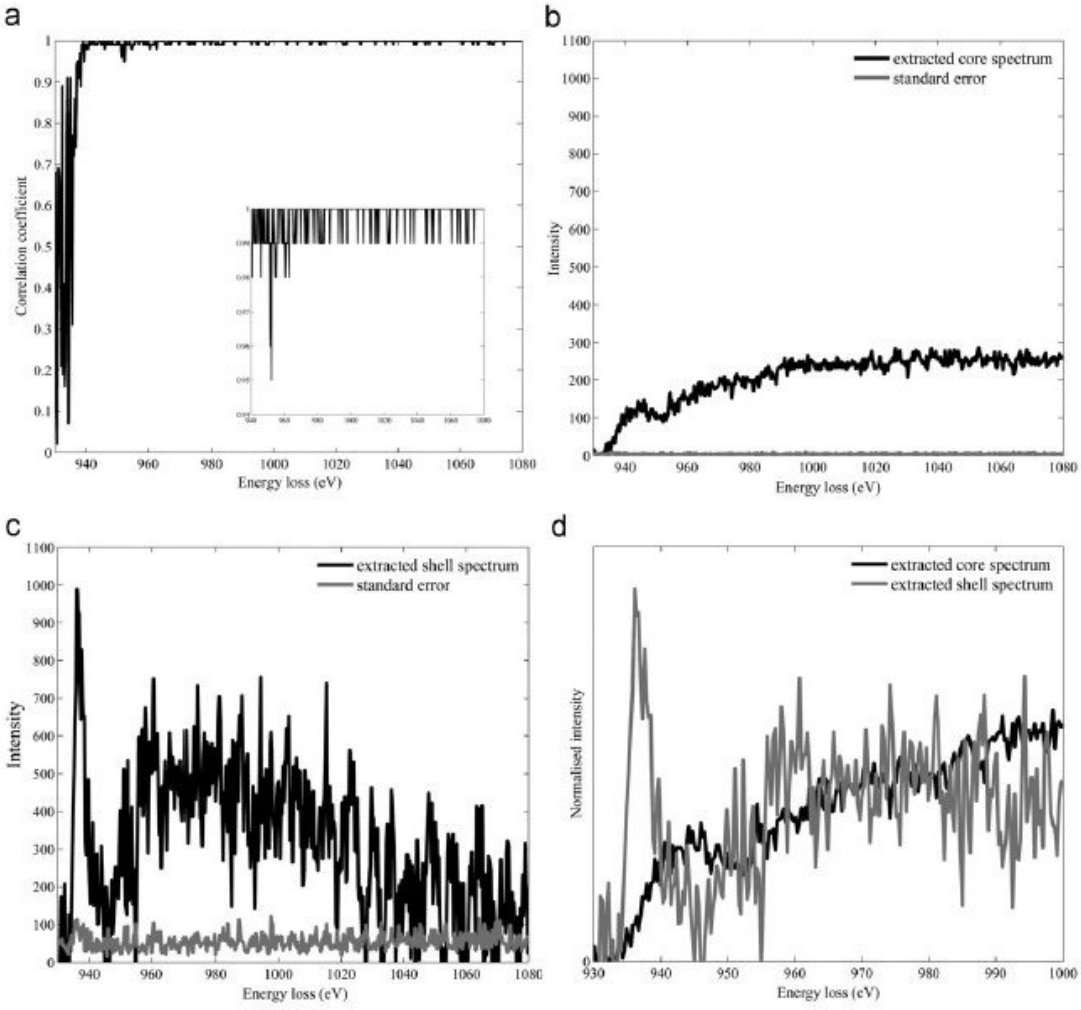
a
Correlation coefficient
Energy loss (eV)
b
extracted core spectrum
standard error
Intensity
Energy loss (eV)
c
extracted shell spectrum
standard error
Intensity
Energy loss (eV)
d
extracted core spectrum
extracted shell spectrum
Normalised intensity
Energy loss (eV)

Figure 10

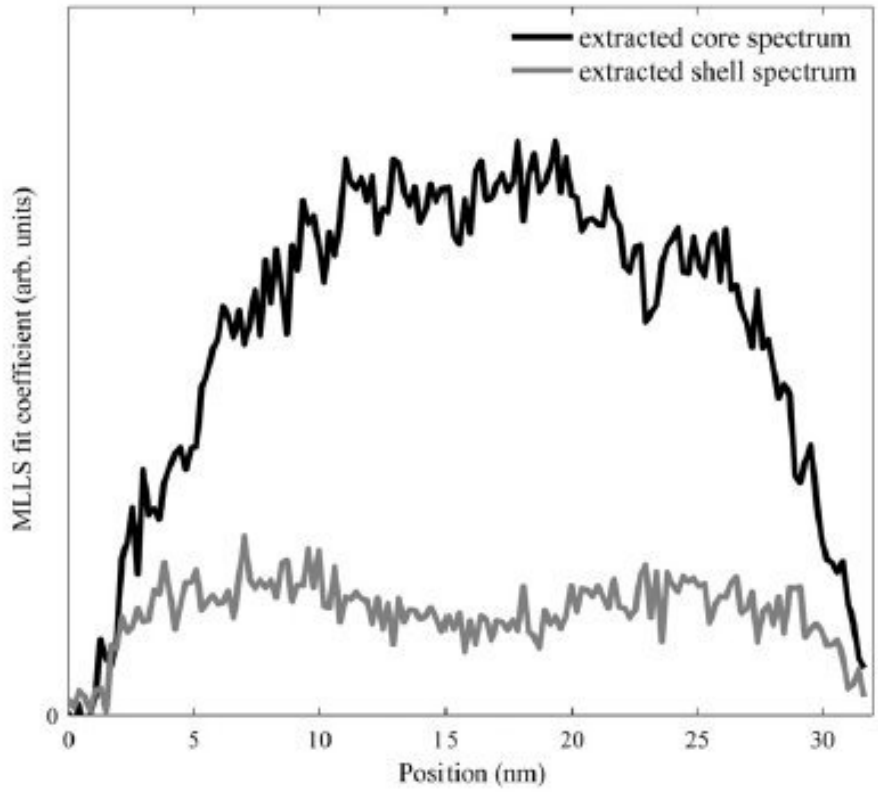
extracted core spectrum
extracted shell spectrum
MLLS fit coefficient (arb. units)
0
0
5
10
15
20
25
30
Position (nm)

Figure 11

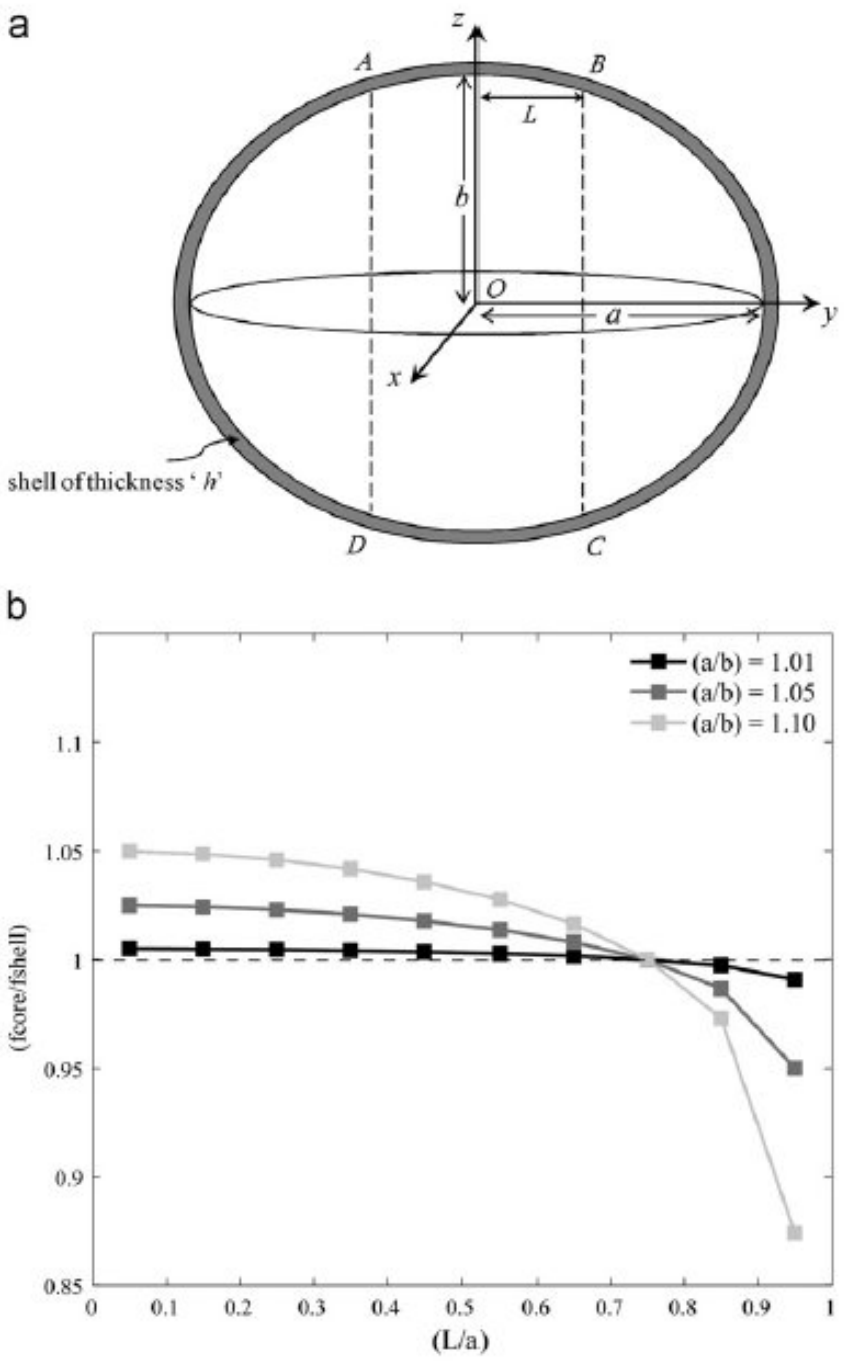
a
z
A
B
L
b
O
a
y
x
shell of thickness ' h'
D
C
b
(a/b) = 1.01
(a/b) = 1.05
(a/b) = 1.10
(fcore/fshell)
1.1
1.05
1
0.95
0.9
0.85
0
0.1
0.2
0.3
0.4
0.5
0.6
0.7
0.8
0.9
1
(L/a)

Figure 12

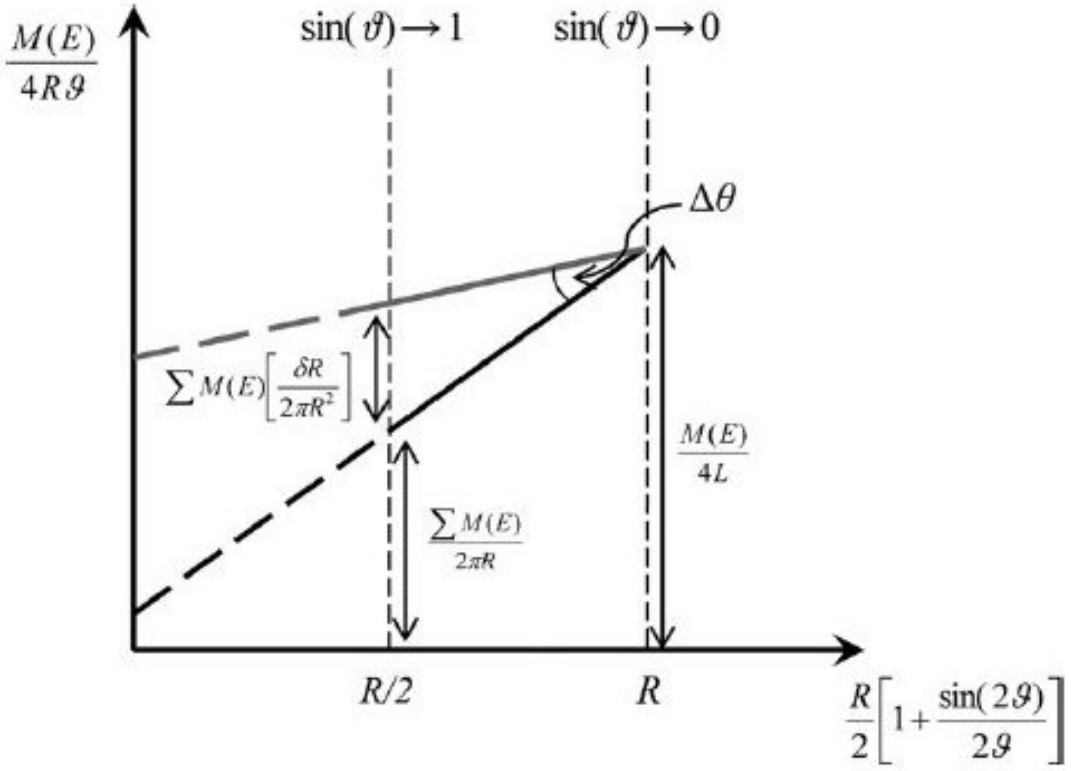
$\frac{M(E)}{4R\vartheta}$
$\sin(\vartheta)\to 1$
$\sin(\vartheta)\to 0$
$\Delta\theta$
$\sum M(E)\left[\frac{\delta R}{2\pi R^2}\right]$
$\frac{M(E)}{4L}$
$\frac{\sum M(E)}{2\pi R}$
$R/2$
$R$
$\frac{R}{2}\left[1+\frac{\sin(2\vartheta)}{2\vartheta}\right]$

Figure 13